

# WaveMamba: Spatial-Spectral Wavelet Mamba for Hyperspectral Image Classification

Muhammad Ahmad, Muhammad Usama, Manual Mazzara

**Abstract**—Hyperspectral Imaging (HSI) has proven to be a powerful tool for capturing detailed spectral and spatial information across diverse applications. Despite the advancements in Deep Learning (DL) and Transformer architectures for HSI Classification (HSIC), challenges such as computational efficiency and the need for extensive labeled data persist. This paper introduces WaveMamba, a novel approach that integrates wavelet transformation with the Spatial-Spectral Mamba architecture to enhance HSIC. WaveMamba captures both local texture patterns and global contextual relationships in an end-to-end trainable model. The Wavelet-based enhanced features are then processed through the state-space architecture to model spatial-spectral relationships and temporal dependencies. The experimental results indicate that WaveMamba surpasses existing models, achieving an accuracy improvement of 4.5% on the University of Houston dataset and a 2.0% increase on the Pavia University dataset. These findings validate its effectiveness in addressing the complex data interactions inherent in HSIs. The source code will be made public at <https://github.com/mahmad00>.

**Index Terms**—Hyperspectral Imaging, Spatial-Spectral Mamba, Wavelets; Hyperspectral Image Classification

## I. INTRODUCTION

**H**YPERSPECTRAL Imaging (HSI) has emerged as a robust technique, capturing contiguous spectral information across various wavelengths. Its applications span in diverse fields such as remote sensing [1], Earth observation, urban planning, agriculture, forestry, target/object detection, mineral exploration, environmental and climate monitoring [2]–[4], forensic sciences [5], [6], and even food, meat, and bakery processing [7]–[11]. HSI is noted for capturing detailed spatial and spectral information, though its high spectral resolution sensors may struggle with optimal spatial resolution in complex scenarios. The extensive spectral data in HSIs presents significant challenges and opportunities for effective classification [1].

Recent advancements in Deep Learning (DL) have significantly improved HSI Classification (HSIC), with Convolutional Neural Networks (CNNs) capturing essential spatial and spectral features for accurate classification [12]–[14]. However, their reliance on local receptive fields and substantial labeled data highlights the need for more advanced architectures to better exploit global context [15], [16]. Meanwhile, Transformer architecture has further advanced HSIC by effectively capturing long-range dependencies and global

contextual information, often surpassing traditional DL models [17]–[23] (Comparative Methods). Despite these improvements, Transformers face challenges related to computational efficiency and the need for extensive labeled data, limiting their practical application in HSIC [23]–[29] (Comparative Methods).

Recently, Mamba architecture, inspired by control theory's State Space Model, achieved linear complexity scaling with sequence length, enhancing HSIC efficiency [30]. Yao et al. [31] introduced SpectralMamba, integrating Mamba with DL techniques through a Gated Spatial-Spectral Merging (GSSM) module and a Piece-wise Sequential Scanning (PSS) strategy. Huang et al. [32] proposed the Spatial-Spectral Mamba (SSMamba) architecture, utilizing spectral-spatial token generation and multiple stacked Mamba blocks for feature fusion, though further optimization is needed. Wang et al. [33] introduced the  $S^2$ Mamba architecture, merging spatial and spectral features with a Spatial-Spectral Mixture Gate to enhance accuracy, but requiring further optimization for complex interactions. He et al. [34] developed the 3D-Spectral-Spatial Mamba (3DSS-Mamba) architecture, capturing global dependencies while maintaining linear complexity, though optimization is needed for high-dimensional data.

To address the aforementioned issues, this paper proposes WaveMamba: a novel approach that combines the strengths of wavelet transformation and the Spatial-Spectral Mamba architecture for improved HSIC. WaveMamba introduces wavelet-enhanced spatial-spectral feature extraction within the Mamba architecture, enhancing the interaction between spectral and spatial information. This results in more accurate classification compared to traditional DL methods. By extracting wavelet-based spatial-spectral features from the HSI data and inputting them into the Mamba architecture, WaveMamba captures both local and global relationships in the data, leading to improved classification accuracy. In this paper, we made the following contributions:

- 1) This paper presents WaveMamba, a novel method that synergistically combines wavelet transformation with Spatial-Spectral Mamba for HSIC. By leveraging wavelet-based multi-resolution analysis, WaveMamba effectively enhances the interaction between spectral and spatial information, thereby capturing a comprehensive range of data critical for accurate HSIC.
- 2) We extract spatial-spectral features from the HSI cube and process them through the Mamba architecture. Overlapping 3D patches together with wavelets improves local feature extraction, capturing fine-grained details. Additionally, a gate mechanism with fully connected dense and non-linear activation layers refines spatial and

M. Ahmad and M. Usama are with the Department of Computer Science, National University of Computer and Emerging Sciences, Islamabad, Chiniot-Faisalabad Campus, Chiniot 35400, Pakistan. (e-mail: mahmad00@gmail.com)

M. Mazzara is with the Institute of Software Development and Engineering, Innopolis University, Innopolis, 420500, Russia. (e-mail: m.mazzara@innopolis.ru)

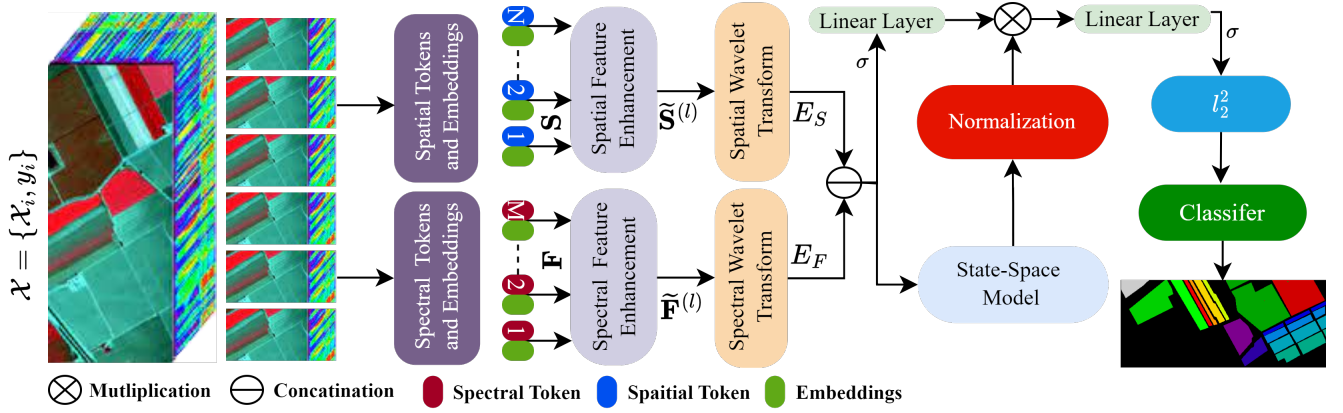


Fig. 1: In WaveMamba, the HSI cube is divided into overlapping 3D patches centered at spatial points, each covering a  $P \times P$  pixel area across all spectral bands. These patches are split into spectral and spatial tokens, enhanced using a spatial-spectral gate mechanism, and transformed with Haar wavelets into four subbands that capture different frequency components and spatial features. The subbands are concatenated into a new 3D representation, which the Mamba architecture uses to capture spatial-spectral relationships and temporal dependencies for classification.

spectral tokens, enhancing feature representation.

- 3) This work also demonstrates that integrating wavelet-based feature extraction with the Mamba architecture's spatial-spectral relationship modeling achieves superior accuracy compared to traditional DL, Transformers, and Mamba methods for HSIC. Furthermore, incorporating the State-Space Model captures temporal dependencies within HSI data, while  $L_2$  regularization in the final classification stage ensures model simplicity and generalizability, reducing overfitting and enhancing performance on unseen data.

## II. PROPOSED METHODOLOGY

An HSI cube  $\mathcal{X} = \{\mathcal{X}_i, y_i\} \in \mathcal{R}^{(H \times W \times C)}$  consists of spectral vectors  $\mathcal{X}_i = \{\mathcal{X}_{i,1}, \mathcal{X}_{i,2}, \mathcal{X}_{i,3}, \dots, \mathcal{X}_{i,C}\}$ , and  $y_i$  corresponding class label of  $\mathcal{X}_i$ . The cube is divided into overlapping 3D patches centered at coordinates  $(\alpha, \beta)$ , each covering  $P \times P$  pixels across  $C^*$  bands. The total number of patches  $N$  is  $(H - P + 1) \times (W - P + 1)$ , where a patch  $P_{\alpha, \beta}$  spans  $\alpha \pm \frac{P-1}{2}$  and  $\beta \pm \frac{P-1}{2}$  in spatial dimensions. The input shape is  $(N, P, P, C^*)$ , with  $C^*$  representing the reduced number of bands. These patches are divided into spectral and spatial components to generate spectral tokens  $\mathbf{F}$  and spatial tokens  $\mathbf{S}$ . By transforming 2D spatial data into  $\mathbf{S}$  and 1D spectral data into  $\mathbf{F}$ , the model captures complex spatial-spectral relationships. The spatial and spectral tokens,  $\mathbf{S}$  and  $\mathbf{F}$ , are generated as follows:

$$\mathbf{S} = [\mathbf{s}_1, \mathbf{s}_2, \dots, \mathbf{s}_C] \in \mathbb{R}^{B \times (HW) \times C} \quad (1)$$

$$\mathbf{F} = [\mathbf{f}_1, \mathbf{f}_2, \dots, \mathbf{f}_{HW}] \in \mathbb{R}^{B \times (HW) \times C} \quad (2)$$

Spatial-spectral feature enhancement is subsequently performed which refines the HSI data features by processing the spatial  $\mathbf{S}$  and spectral  $\mathbf{F}$  tokens using a "spatial and spectral gate" mechanism. This mechanism involves fully connected dense layers, non-linear activation functions, and reshaped layers. The spatial gate enhances the spatial tokens  $\mathbf{S}$ , and the spectral gate enhances the spectral tokens  $\mathbf{F}$ . This process

results in improved spatial and spectral token representations for subsequent analysis.

$$\tilde{\mathbf{S}}^{(l)} = \mathbf{S}^{(l)} \odot \sigma(\mathbf{W}_s \mathbf{c} + \mathbf{b}_s) \quad (3)$$

$$\tilde{\mathbf{F}}^{(l)} = \mathbf{F}^{(l)} \odot \sigma(\mathbf{W}_f \mathbf{c} + \mathbf{b}_f) \quad (4)$$

where  $W_s$  and  $W_f$  are learned weights and  $\sigma$  is the sigmoid function.

The enhanced spatial-spectral feature map  $\tilde{\mathbf{S}}^{(l)}$  and  $\tilde{\mathbf{F}}^{(l)}$  are transformed into  $\hat{\mathbf{S}}^{(l)}$  and  $\hat{\mathbf{F}}^{(l)}$  i.e.,  $\hat{\mathbf{S}}^{(l)}$  and  $\hat{\mathbf{F}}^{(l)} \in \mathcal{R}^{H \times W \times C^*}$  decomposed into 4 wavelet sub-channels which is down-sampled through wavelet transformation. Note that, here we used the classical Haar wavelet as expressed in [35], [36]. Concretely, the wavelet transformation is applied using a lowpass filter, denoted as  $f_l = \left(\frac{1}{\sqrt{2}}, \frac{1}{\sqrt{2}}\right)$ , and a highpass filter, denoted as  $f_h = \left(\frac{1}{\sqrt{2}}, -\frac{1}{\sqrt{2}}\right)$ , along the rows of the input spatial and spectral features  $\hat{\mathbf{S}}^{(l)}$  and  $\hat{\mathbf{F}}^{(l)}$ . This process results in the creation of four sub-channels, namely  $\hat{\mathbf{S}}_l^{(l)}$ ,  $\hat{\mathbf{S}}_h^{(l)}$  (Spatial) and  $\hat{\mathbf{F}}_l^{(l)}$ ,  $\hat{\mathbf{F}}_h^{(l)}$  (Spectral). Subsequently, the same lowpass filter  $f_l$  and highpass filter  $f_h$  are employed, this time along the columns of the derived sub-channels. This leads to the formation of eight sub-channels in total:  $\hat{\mathbf{S}}_{ll}^{(l)}$ ,  $\hat{\mathbf{S}}_{lh}^{(l)}$ ,  $\hat{\mathbf{S}}_{hl}^{(l)}$ , and  $\hat{\mathbf{S}}_{hh}^{(l)}$  for spatial information and similarly  $\hat{\mathbf{F}}_{ll}^{(l)}$ ,  $\hat{\mathbf{F}}_{lh}^{(l)}$ ,  $\hat{\mathbf{F}}_{hl}^{(l)}$ , and  $\hat{\mathbf{F}}_{hh}^{(l)}$  for spectral information. Each of these wavelet subbands can be viewed as a down-sampled version of the original input  $\tilde{\mathbf{S}}^{(l)}$  and  $\tilde{\mathbf{F}}^{(l)}$ . They collectively preserve all the input details without any loss of information. The wavelet process is explained in Algorithm 1.

The wavelet features are linearly transformed into the state-space model. Given a sequence of wavelet features  $O = (E_1, E_2, E_3, \dots, E_T)$ , the state transition is computed as:

$$h_t = \text{ReLU}(W_{\text{transition}} h_{t-1} + W_{\text{update}} E_t) \quad (5)$$

where  $W_{\text{transition}}$  and  $W_{\text{update}}$  are learned weights, and  $h_t$  is the hidden state at time  $t$ . The final output is obtained by applying a linear classifier to  $h_t$ :

$$y = \sigma(h_t W_{\text{classifier}}) \quad (6)$$

---

**Algorithm 1: Wavelet Transformation**


---

**Input:**  $\tilde{\mathbf{S}}^{(l)}, \tilde{\mathbf{F}}^{(l)}$ 

- 1 Convert  $\tilde{\mathbf{S}}^{(l)}$  and  $\tilde{\mathbf{F}}^{(l)}$  to NumPy array  $\tilde{\mathbf{S}}_{np}^{(l)}$  and  $\tilde{\mathbf{F}}_{np}^{(l)}$ ;
  - 2 Initialize empty output arrays  $E_S$  and  $E_F$ ;
  - 3 Apply Discrete Wavelet Transform (DWT) on  $\tilde{\mathbf{S}}_{np}^{(l)}$  and  $\tilde{\mathbf{F}}_{np}^{(l)}$  using 'haar' wavelet;
  - 4 Extract approximation and detail coefficients  $(\hat{\mathbf{S}}_{ll}^{(l)}, \hat{\mathbf{S}}_{lh}^{(l)}, \hat{\mathbf{S}}_{hl}^{(l)}, \hat{\mathbf{S}}_{hh}^{(l)})$  and  $(\hat{\mathbf{F}}_{ll}^{(l)}, \hat{\mathbf{F}}_{lh}^{(l)}, \hat{\mathbf{F}}_{hl}^{(l)}, \hat{\mathbf{F}}_{hh}^{(l)})$  from DWT;
  - 5 Combine coefficients by concatenating  $E_S \leftarrow \hat{\mathbf{S}}_{ll}^{(l)}, \hat{\mathbf{S}}_{lh}^{(l)}, \hat{\mathbf{S}}_{hl}^{(l)}, \hat{\mathbf{S}}_{hh}^{(l)}$  and  $E_F \leftarrow \hat{\mathbf{F}}_{ll}^{(l)}, \hat{\mathbf{F}}_{lh}^{(l)}, \hat{\mathbf{F}}_{hl}^{(l)}, \hat{\mathbf{F}}_{hh}^{(l)}$ ;
  - 6 Reshape combined coefficients individually ( $E_S$  and  $E_F$ ) to maintain 3D shape;
  - 7 Convert Transformed back to tensors as  $E_S$  and  $E_F$ ;
  - 8 Concatenate  $E_S$  and  $E_F$  as  $E$ ;
  - 9 Return  $E$ ;
- 

where  $\|W_{\text{classifier}}\|_2^2$  is the squared  $l_2$  norm of  $W_{\text{classifier}}$ . The regularization coefficient  $\lambda = 0.01$  controls the strength of regularization, with  $\sigma$  denoting the sigmoid function for classification.  $l_2$  regularization penalizes large values in  $W_{\text{classifier}}$ , promoting simpler models and preventing overfitting. This approach allows WaveMamba to effectively utilize both spatial and spectral information, improving its classification of HSI data by integrating insights from both modalities.

### III. EXPERIMENTAL RESULTS AND DISCUSSION

This section presents the results from testing on the University of Houston and Pavia University HSI datasets, where the model, trained over 50 epochs with Adam optimizer and a 0.001 learning rate, effectively learned patterns using a mini-batch size of 256, Mamba block embeddings of 64, state space dimensions of 128, and a 0.1 dropout rate with  $l_2^2$  regularization. The model weights were randomly initialized and fine-tuned, achieving improved performance.

#### A. Patch Size and Train-Validation-Test Samples

The effects of training sample percentage and patch size on model performance were evaluated to determine the optimal configuration. Table I shows that varying training percentages with a fixed  $4 \times 4$  patch size and testing different patch sizes reveal that smaller patches capture fine details but may overfit due to noise sensitivity. Larger patches, in contrast, capture global features, improving robustness and generalization as sample sizes increase. Optimal patch size depends on dataset size: larger patches benefit smaller datasets, while smaller patches are better for larger ones. Increasing the training set size generally enhances performance, especially with larger patches, by improving pattern learning and reducing overfitting. A balanced validation sample size is crucial for effective hyperparameter tuning, as very small or very large sets can lead to suboptimal results or excessive computation. Finally, very small test sets may not reliably estimate WaveMamba's generalization capability.

TABLE I: Performance of WaveMamba with Different Patch Sizes and Various Training Percentages (%)

Train %	AA	OA	$\kappa$	Tr Time	Patch Size	AA	OA	$\kappa$	Tr Time (s)
Pavia University									
5%	93.11	95.79	94.43	445.35	$2 \times 2$	93.85	95.64	94.21	1407.88
10%	95.63	97.39	96.54	805.27	$4 \times 4$	97.17	98.15	97.55	1586.50
15%	96.58	97.85	97.15	1064.72	$6 \times 6$	96.42	97.51	96.70	1764.15
20%	97.13	98.19	97.61	1704.64	$8 \times 8$	<b>97.87</b>	<b>98.67</b>	<b>98.23</b>	1917.34
25%	<b>97.87</b>	<b>98.67</b>	<b>98.23</b>	1917.34	$10 \times 10$	95.75	97.38	96.53	2149.22
University of Houston									
5%	88.43	91.26	90.54	98.83	$2 \times 2$	97.01	97.57	97.38	1003.88
10%	94.98	96.18	95.87	199.04	$4 \times 4$	<b>98.15</b>	<b>98.48</b>	<b>98.35</b>	1043.73
15%	96.22	96.92	96.66	293.63	$6 \times 6$	96.37	97.39	97.17	1103.58
20%	96.96	97.71	97.52	444.91	$8 \times 8$	97.96	97.99	97.82	747.63
25%	<b>98.15</b>	<b>98.48</b>	<b>98.35</b>	1043.73	$10 \times 10$	97.41	97.60	97.41	864.75

#### B. Experimental Results with CNN-based Models

A consistent experimental methodology was employed for fair model comparison using unique sample distributions, spatial locations, and a controlled  $10 \times 10$  pixel patch size. Figure 2 illustrates the loss and accuracy trends on the University of Houston dataset, while ground truth maps for WaveMamba and other models are shown in Figures 3 and 4. The evaluated models include 2D CNN, 3D CNN, Hybrid Inception Net, 3D Inception Net, 2D Inception Net, and Hybrid CNN. The results demonstrate the benefits of decoupling spatial and spectral information with Wavelets in WaveMamba, which achieved impressive scores of 97%, comparable to CNN models. The marginal accuracy difference between WaveMamba and other CNN-based methods is likely due to WaveMamba's computational efficiency, reduced overfitting, and improved modeling of spatial and spectral dependencies, with similar trends observed for the Pavia University dataset.

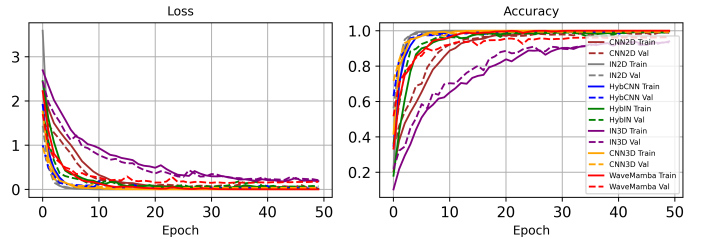


Fig. 2: The comparison above illustrates the accuracy and loss trends of CNN-based methods. The WaveFormer (represented by the red line) demonstrates quicker convergence than traditional CNN models.

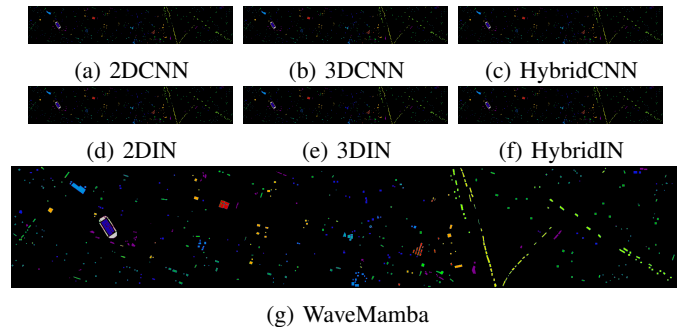


Fig. 3: **University of Houston:** The proposed WaveMamba achieves OA=97.30% showing competitive performance. All these results are compiled using  $10 \times 10$  patch size with 25% training samples for all competing methods.

TABLE II: Per Class classification accuracy (Overall (OA) and Average Accuracy (AA) %) and Kappa ( $\kappa$ ) measure for **University of Houston**. (WM = WaveMamba).

Class	[17]	[18]	[19]	[23]	[21]	[22]	[37]	[24]	[25]	[27]	[26]	[20]	[28]	[29]	[38]	WM
1	93.31	97.26	93.39	97.24	83.00	88.13	81.23	80.51	79.47	93.44	93.48	95.36	92.67	90.90	92.88	97.92
2	97.81	97.29	99.54	97.69	83.74	90.04	87.59	67.45	79.08	95.37	95.10	98.58	97.57	95.11	95.99	98.72
3	100.0	98.74	100.0	97.76	89.70	100.0	88.19	99.12	100.0	98.67	100.0	99.20	98.17	97.10	100.0	100.0
4	100.0	95.78	98.09	97.85	92.57	89.49	77.05	97.39	98.51	97.69	97.13	97.82	96.58	92.27	99.17	98.39
5	98.16	98.41	97.70	99.91	99.81	98.20	90.09	96.64	100.0	98.61	97.66	99.99	99.78	98.58	98.29	99.67
6	100.00	91.36	100.0	92.46	100.0	99.30	93.94	84.66	87.53	95.08	97.37	98.42	97.47	96.42	96.39	93.82
7	87.83	94.60	90.96	90.70	87.59	98.97	87.53	78.78	77.00	91.46	91.93	84.32	86.43	89.18	91.60	87.85
8	85.91	91.82	89.18	96.78	73.22	98.01	93.02	45.49	49.77	78.02	94.88	80.80	83.25	83.90	83.33	97.42
9	75.33	92.39	90.62	94.85	81.21	95.94	86.12	76.05	72.19	92.26	88.57	78.82	82.61	86.58	92.05	91.69
10	82.52	90.61	93.22	99.27	68.15	98.65	78.68	36.93	94.51	97.61	89.76	95.10	96.50	99.09	98.05	98.20
11	79.19	89.09	87.91	96.13	89.85	87.38	81.65	64.05	85.59	93.82	95.44	95.82	93.46	92.34	92.48	96.27
12	72.76	94.18	83.15	99.18	89.15	94.33	89.71	70.01	59.63	92.45	93.15	89.65	89.55	91.27	91.24	98.70
13	79.49	82.51	84.11	65.16	92.28	98.95	85.49	98.81	80.06	95.86	82.75	97.75	92.98	91.22	92.87	82.90
14	93.90	91.55	97.21	98.96	100.0	98.79	93.02	99.81	100.0	99.95	98.13	99.85	99.88	100.0	100.0	99.53
15	97.50	96.72	100.0	100.0	100.0	62.16	88.33	96.41	99.57	99.45	99.05	100.0	99.97	98.63	100.0	100.0
OA	88.45	93.06	93.09	96.08	86.30	93.21	86.50	75.65	82.14	93.92	93.67	92.88	92.85	92.73	94.30	<b>96.39</b>
AA	87.81	86.61	92.06	94.93	88.68	93.22	85.25	79.34	84.19	94.65	94.03	94.10	93.79	93.51	94.96	<b>96.07</b>
$\kappa$	87.50	92.50	92.53	95.76	85.14	92.63	85.85	73.73	80.70	93.43	93.16	92.30	92.27	92.14	93.84	<b>96.10</b>

TABLE III: Per Class classification accuracy (Overall (OA) and Average Accuracy (AA) %) and Kappa ( $\kappa$ ) measure for **Pavia University**. (WM = WaveMamba).

Class	[17]	[18]	[19]	[23]	[21]	[22]	[37]	[24]	[25]	[27]	[26]	[20]	[28]	[29]	[38]	WM
1	92.67	95.21	95.25	96.34	90.44	94.75	98.76	78.09	76.94	97.06	98.74	86.16	87.16	90.59	95.70	96.92
2	92.79	92.54	96.64	99.51	96.63	95.54	95.46	84.67	93.70	92.29	99.51	94.50	95.05	94.62	94.05	99.58
3	90.60	91.18	81.74	82.74	93.50	99.83	87.75	53.47	81.10	99.97	90.81	93.94	93.95	94.39	99.61	87.70
4	98.15	97.21	95.50	96.33	90.94	93.99	91.37	75.09	78.42	97.12	92.74	88.97	92.76	84.61	98.92	95.88
5	98.28	100.0	99.59	100.00	98.71	95.82	92.13	99.83	100.0	100.0	99.53	98.95	98.85	99.18	100.0	99.40
6	93.29	99.93	93.43	92.31	98.82	97.32	97.10	52.40	64.24	99.40	90.96	96.07	99.19	99.53	99.19	98.40
7	83.01	95.75	89.24	92.06	98.13	96.58	96.47	78.74	96.27	100.0	93.80	99.58	99.08	99.34	99.93	97.89
8	84.50	97.59	88.81	90.67	93.95	95.37	86.25	84.35	58.58	98.99	89.83	86.63	91.74	97.10	98.50	88.86
9	99.77	99.47	99.53	93.30	95.24	92.18	89.27	99.60	98.16	99.47	96.82	95.54	95.49	93.95	99.96	95.56
OA	92.30	91.35	94.48	96.05	95.25	95.05	94.64	78.23	83.28	95.79	95.87	92.61	94.06	94.33	96.40	<b>96.58</b>
AA	88.86	85.07	93.15	93.71	95.15	93.01	92.78	78.47	83.06	98.25	94.75	93.37	94.81	94.81	<b>98.43</b>	97.11
$\kappa$	89.66	88.94	92.67	94.74	93.55	94.70	93.54	71.55	77.74	94.54	94.58	90.29	92.22	92.60	95.31	<b>96.17</b>

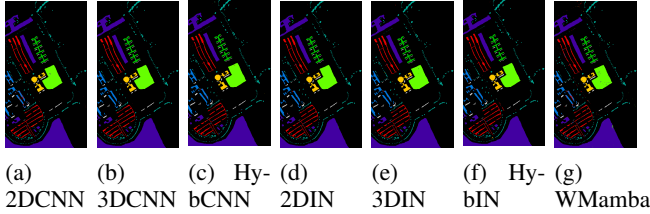


Fig. 4: **Pavia University**: The proposed WaveMamba achieves OA=96.58% showing competitive performance. All these results are compiled using  $10 \times 10$  patch size with 25% training samples for all competing methods.

### C. Comparative Results with Transformer and Mamba Networks

To illustrate the effectiveness of WaveMamba, it was compared against a range of HSIC methods, including Spectralformer (SF) [17], HiT [18], CSiT [19], SSFTT [20], S3L [37], RIAN [21], CAT [22], SPRLT [24], CMT [25], and additional models such as DBDA [26], MSSG [27], LSFAT [28], CT-Mixer [29], SSFormer [23], and SS-Mamba [38]. This diverse set includes advanced CNN models incorporating dual-attention mechanisms, Transformer-based approaches, and hybrid models, thereby providing a comprehensive benchmark for assessing WaveMamba's performance and innovation within HSIC techniques.

The results, as presented in Tables III and II, demonstrate

that WaveMamba surpasses the competing methods in terms of Overall Accuracy (OA), Average Accuracy (AA), and Kappa ( $\kappa$ ) measure on both the Pavia University and University of Houston datasets. Specifically, WaveMamba achieves OA values of 96.58% and 96.39% for the respective datasets, outperforming the second-best method, SS-Mamba, by margins of 0.18% and 2.09%. Furthermore, WaveMamba exhibits superior performance in AA and  $\kappa$  measure, underscoring its robustness and efficacy in HSIC tasks. The per-class classification accuracy results, detailed in Tables III and II, further emphasize WaveMamba's strengths. Notable improvements are observed in classes 3, 6, 8, and 9 on the Pavia University dataset, and in classes 8, 10, 12, and 15 on the University of Houston dataset. These results highlight WaveMamba's capability to accurately classify a variety of land cover types, affirming its potential as a promising approach for HSIC applications.

## IV. CONCLUSIONS

This paper introduced "WaveMamba," which integrates wavelet transformation with the Spatial-Spectral Mamba architecture for HSIC. By leveraging wavelet-based extraction of multi-scale spatial-spectral features, WaveMamba captures both local texture patterns and global contextual relationships in an end-to-end trainable model. A key innovation is the incorporation of a State-Space Model, enhancing the modeling of temporal dependencies alongside spatial-spectral

information. Extensive experiments show that WaveMamba significantly improves classification accuracy over well-known advanced DL methods, especially in datasets with limited training data, by effectively capturing nuanced spectral and structural details. The method not only achieves superior performance but also demonstrates robustness and generalizability, making it a promising solution for real-world HSIC challenges. Future work could focus on exploring self-supervised pre-training and further network optimizations to enhance WaveMamba's performance in data-scarce environments.

## REFERENCES

- [1] M. Ahmad, S. Shabbir, S. K. Roy, D. Hong, X. Wu, J. Yao, A. M. Khan, M. Mazzara, S. Distefano, and J. Chanussot, "Hyperspectral image classification—traditional to deep models: A survey for future prospects," *IEEE Journal of Selected Topics in Applied Earth Observations and Remote Sensing*, 2021.
- [2] C. Weber, R. Aguejda, X. Briottet, J. Avala, S. Fabre, J. Demuynck, E. Zenou, Y. Deville, M. S. Karoui, F. Z. Benhalouche *et al.*, "Hyperspectral imagery for environmental urban planning," in *IGARSS 2018-2018 IEEE International Geoscience and Remote Sensing Symposium*. IEEE, 2018, pp. 1628–1631.
- [3] M. B. Stuart, A. J. McGonigle, and J. R. Willmott, "Hyperspectral imaging in environmental monitoring: A review of recent developments and technological advances in compact field deployable systems," *Sensors*, vol. 19, no. 14, p. 3071, 2019.
- [4] C. B. Pande and K. N. Moharir, "Application of hyperspectral remote sensing role in precision farming and sustainable agriculture under climate change: A review," *Climate Change Impacts on Natural Resources, Ecosystems and Agricultural Systems*, pp. 503–520, 2023.
- [5] M. H. F. Butt, H. Ayaz, M. Ahmad, J. P. Li, and R. Kuleev, "A fast and compact hybrid cnn for hyperspectral imaging-based bloodstain classification," in *2022 IEEE Congress on Evolutionary Computation (CEC)*. IEEE, 2022, pp. 1–8.
- [6] M. Zulfiqar, M. Ahmad, A. Sohaib, M. Mazzara, and S. Distefano, "Hyperspectral imaging for bloodstain identification," *Sensors*, vol. 21, no. 9, p. 3045, 2021.
- [7] M. H. Khan, Z. Saleem, M. Ahmad, A. Sohaib, H. Ayaz, M. Mazzara, and R. A. Raza, "Hyperspectral imaging-based unsupervised adulterated red chili content transformation for classification: Identification of red chili adulterants," *Neural Computing and Applications*, vol. 33, no. 21, pp. 14 507–14 521, 2021.
- [8] M. H. Khan, Z. Saleem, M. Ahmad, A. Sohaib, H. Ayaz, and M. Mazzara, "Hyperspectral imaging for color adulteration detection in red chili," *Applied Sciences*, vol. 10, no. 17, p. 5955, 2020.
- [9] Z. Saleem, M. H. Khan, M. Ahmad, A. Sohaib, H. Ayaz, and M. Mazzara, "Prediction of microbial spoilage and shelf-life of bakery products through hyperspectral imaging," *IEEE Access*, vol. 8, pp. 176 986–176 996, 2020.
- [10] H. Ayaz, M. Ahmad, M. Mazzara, and A. Sohaib, "Hyperspectral imaging for minced meat classification using nonlinear deep features," *Applied Sciences*, vol. 10, no. 21, p. 7783, 2020.
- [11] H. Ayaz, M. Ahmad, A. Sohaib, M. N. Yasir, M. A. Zaidan, M. Ali, M. H. Khan, and Z. Saleem, "Myoglobin-based classification of minced meat using hyperspectral imaging," *Applied Sciences*, vol. 10, no. 19, p. 6862, 2020.
- [12] D. Hong, J. Yao, C. Li, D. Meng, N. Yokoya, and J. Chanussot, "Decoupled-and-coupled networks: Self-supervised hyperspectral image super-resolution with subpixel fusion," *IEEE Transactions on Geoscience and Remote Sensing*, 2023.
- [13] M. Ahmad, A. M. Khan, M. Mazzara, S. Distefano, M. Ali, and M. S. Sarfraz, "A fast and compact 3-d cnn for hyperspectral image classification," *IEEE Geoscience and Remote Sensing Letters*, 2020.
- [14] U. Ghous, M. S. Sarfraz, M. Ahmad, C. Li, and D. Hong, "(2+1)d extreme xception net for hyperspectral image classification," *IEEE Journal of Selected Topics in Applied Earth Observations and Remote Sensing*, pp. 1–14, 2024.
- [15] D. Hong, B. Zhang, X. Li, Y. Li, C. Li, J. Yao, N. Yokoya, H. Li, P. Ghamisi, X. Jia, A. Plaza, P. Gamba, J. A. Benediktsson, and J. Chanussot, "Spectralgpt: Spectral remote sensing foundation model," *IEEE Transactions on Pattern Analysis and Machine Intelligence*, 2024, doi:10.1109/TPAMI.2024.3362475.
- [16] M. Ahmad and M. Mazzara, "Scsnet: Sharpened cosine similarity-based neural network for hyperspectral image classification," *IEEE Geoscience and Remote Sensing Letters*, vol. 21, pp. 1–4, 2024.
- [17] D. Hong, Z. Han, J. Yao, L. Gao, B. Zhang, A. Plaza, and J. Chanussot, "Spectralformer: Rethinking hyperspectral image classification with transformers," *IEEE Trans. Geosci. Remote Sens.*, vol. 60, pp. 1–15, 2022, doi: 10.1109/TGRS.2021.3130716.
- [18] X. Yang, W. Cao, Y. Lu, and Y. Zhou, "Hyperspectral image transformer classification networks," *IEEE Transactions on Geoscience and Remote Sensing*, vol. 60, pp. 1–15, 2022.
- [19] W. He, W. Huang, S. Liao, Z. Xu, and J. Yan, "Csit: A multiscale vision transformer for hyperspectral image classification," *IEEE Journal of Selected Topics in Applied Earth Observations and Remote Sensing*, vol. 15, pp. 9266–9277, 2022.
- [20] L. Sun, G. Zhao, Y. Zheng, and Z. Wu, "Spectral-spatial feature tokenization transformer for hyperspectral image classification," *IEEE Transactions on Geoscience and Remote Sensing*, vol. 60, pp. 1–14, 2022.
- [21] X. Zheng, H. Sun, X. Lu, and W. Xie, "Rotation-invariant attention network for hyperspectral image classification," *IEEE Transactions on Image Processing*, vol. 31, pp. 4251–4265, 2022.
- [22] J. Feng, Q. Wang, G. Zhang, X. Jia, and J. Yin, "Cat: Center attention transformer with stratified spatial-spectral token for hyperspectral image classification," *IEEE Transactions on Geoscience and Remote Sensing*, vol. 62, pp. 1–15, 2024.
- [23] M. Ahmad, M. Usama, A. M. Khan, S. Distefano, H. A. Altuwaijri, and M. Mazzara, "Spatial spectral transformer with conditional position encoding for hyperspectral image classification," *IEEE Geoscience and Remote Sensing Letters*, pp. 1–1, 2024.
- [24] Z. Xue, Q. Xu, and M. Zhang, "Local transformer with spatial partition restore for hyperspectral image classification," *IEEE Journal of Selected Topics in Applied Earth Observations and Remote Sensing*, vol. 15, pp. 4307–4325, 2022.
- [25] S. Jia, Y. Wang, S. Jiang, and R. He, "A center-masked transformer for hyperspectral image classification," *IEEE Transactions on Geoscience and Remote Sensing*, vol. 62, pp. 1–16, 2024.
- [26] R. Li, S. Zheng, C. Duan, Y. Yang, and X. Wang, "Classification of hyperspectral image based on double-branch dual-attention mechanism network," *Remote Sensing*, vol. 12, no. 3, 2020. [Online]. Available: <https://www.mdpi.com/2072-4292/12/3/582>
- [27] Q. Liu, L. Xiao, J. Yang, and Z. Wei, "Multilevel superpixel structured graph u-nets for hyperspectral image classification," *IEEE Transactions on Geoscience and Remote Sensing*, vol. 60, pp. 1–15, 2022.
- [28] B. Tu, X. Liao, Q. Li, Y. Peng, and A. Plaza, "Local semantic feature aggregation-based transformer for hyperspectral image classification," *IEEE Transactions on Geoscience and Remote Sensing*, vol. 60, pp. 1–15, 2022.
- [29] J. Zhang, Z. Meng, F. Zhao, H. Liu, and Z. Chang, "Convolution transformer mixer for hyperspectral image classification," *IEEE Geoscience and Remote Sensing Letters*, vol. 19, pp. 1–5, 2022.
- [30] A. Gu and T. Dao, "Mamba: Linear-time sequence modeling with selective state spaces," *arXiv preprint arXiv:2312.00752*, 2023.
- [31] J. Yao, D. Hong, C. Li, and J. Chanussot, "Spectralmamba: Efficient mamba for hyperspectral image classification," 2024. [Online]. Available: <https://arxiv.org/abs/2404.08489>
- [32] L. Huang, Y. Chen, and X. He, "Spectral-spatial mamba for hyperspectral image classification," *arXiv preprint arXiv:2404.18401*, 2024.
- [33] G. Wang, X. Zhang, Z. Peng, T. Zhang, X. Jia, and L. Jiao, "S<sup>2</sup> mamba: A spatial-spectral state space model for hyperspectral image classification," *arXiv preprint arXiv:2404.18213*, 2024.
- [34] Y. He, B. Tu, B. Liu, J. Li, and A. Plaza, "3dss-mamba: 3d-spectral-spatial mamba for hyperspectral image classification," *arXiv preprint arXiv:2405.12487*, 2024.
- [35] P. Liu, H. Zhang, K. Zhang, L. Lin, and W. Zuo, "Multi-level wavelet-cnn for image restoration," in *Proceedings of the IEEE conference on computer vision and pattern recognition workshops*, 2018, pp. 773–782.
- [36] S. Fujieda, K. Takayama, and T. Hachisuka, "Wavelet convolutional neural networks," 2018.
- [37] H. Guo and W. Liu, "S3l: Spectrum transformer for self-supervised learning in hyperspectral image classification," *Remote Sensing*, vol. 16, no. 6, 2024.
- [38] L. Huang, Y. Chen, and X. He, "Spectral-spatial mamba for hyperspectral image classification," *Remote Sensing*, vol. 16, no. 13, 2024.